

Adversarial Transformer for Repairing Human Airway Segmentation

Zeyu Tang, Nan Yang, Simon Walsh and Guang Yang, *Senior Member, IEEE*

Abstract—Discontinuity in the delineation of peripheral bronchioles hinders the potential clinical application of automated airway segmentation models. Moreover, the deployment of such models is limited by the data heterogeneity across different centres, and pathological abnormalities also make achieving accurate robust segmentation in distal small airways difficult. Meanwhile, the diagnosis and prognosis of lung diseases often rely on evaluating structural changes in those anatomical regions. To address this gap, this paper presents a patch-scale adversarial-based refinement network that takes in preliminary segmentation along with original CT images and outputs a refined mask of the airway structure. The method is validated on three different datasets encompassing healthy cases, cases with cystic fibrosis and cases with COVID-19. The results are quantitatively evaluated by seven metrics and achieved more than a 15% rise in detected length ratio and detected branch ratio, showing promising performance compared to previously proposed models. The visual illustration also proves our refinement guided by a patch-scale discriminator and centreline objective functions is effective in detecting discontinuities and missing bronchioles. Furthermore, the generalizability of our refinement pipeline is tested on three previous models and improves their segmentation completeness significantly.

Index Terms—segmentation, airway, GAN, transformer, refinement, explainable

I. INTRODUCTION

AIRWAY segmentation from chest computerised tomography (CT) scan serves an important role in the diagnosis and prognosis of pulmonary diseases. Manual segmentation by radiologists is highly time-consuming and error-prone due to the large volume of CT data and complex airway tree structure. To relieve the radiology experts from these tedious manual labelling processes, many automated and semi-automated algorithms are being developed. The performance of traditional segmentation methods, such as thresholding [1] and region-growing [2][3], have been benchmarked in the EXACT’09 challenge [4], and no algorithm could extract more than an average of 74% of the total tree length. Recent developments

This study was supported in part by the BHF (TG/18/5/34111, PG/16/78/32402), the ERC IMI (101005122), the H2020 (952172), the MRC (MC/PC/21013), the Royal Society (IEC/NSFC/211235), the SABER project supported by Boehringer Ingelheim Ltd, the NVIDIA Academic Hardware Grant Program, and the UKRI Future Leaders Fellowship (MR/V023799/1).

S.Walsh and G.Yang are the co-last senior authors. Send correspondence to Y. Nan and G. Yang

Zeyu Tang and Nan Yang are with the National Heart and Lung Institute, Imperial College London, SW7 2BX London, U.K. Zeyu is also with the Department of Bioengineering, Imperial College London, SW7 2AZ London, U.K. (e-mail: zeyu.tang19@imperial.ac.uk; y.nan20@imperial.ac.uk)

Simon Walsh and Guang Yang are with the National Heart and Lung Institute, Imperial College London, SW7 2BX London, U.K., and also with the Royal Brompton Hospital, SW3 6NP London, U.K. (e-mail: s.walsh@imperial.ac.uk, g.yang@imperial.ac.uk).

in convolutional neural networks inspired researchers to try models such as U-Net [5], 3-D U-Net [6], V-Net [7] and their derivatives [8][9][10] on the airway segmentation problem. However, despite the improvements in Dice score, CNN-based

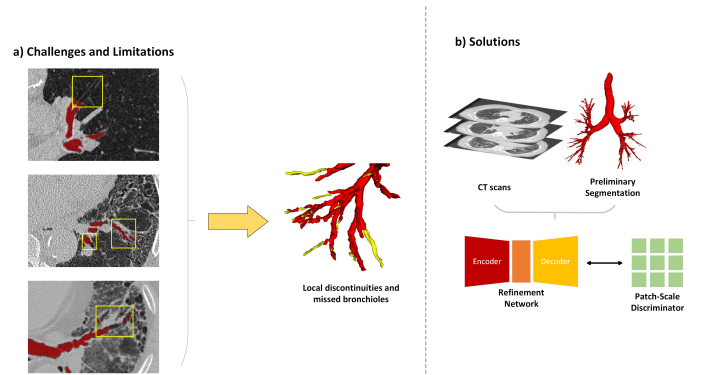


Fig. 1: Current challenges and solutions of airway segmentation. (a) Examples of blurry boundaries, pathological changes and low resolution (indicated in yellow boxes) leading to discontinued segmentation and missing branches highlighted in yellow. (b) This paper proposes an adversarial-based refinement network to help achieve complete and robust airway segmentation. Patch-scale discriminators are incorporated to penalize local structural errors.

models still suffer from local discontinuity, especially in the peripheral region of the lung where there is an enormous imbalance between the target distal small airways and the background. Moreover, these deep neural networks are trained on image patches due to the high computation complexity. The small errors in each patch are hard to notice until these patches are stitched into the full image. Later work from [11], [12] and [13] tried to design specific complex architecture and loss functions to address the discontinuity issue. In addition, the model performance in pathological cases has been neglected. Structural alterations of the lung, such as honeycombing, bronchial wall thickening and bronchiectasis make the model less robust, leading to local discontinuity and missing bronchi or bronchioles in the segmentation. Variable airway branching patterns between individuals and the data heterogeneity across different medical centres and institutes further complicate the challenge.

To tackle these problems, we present in this paper a simple yet effective adversarial-based patch-scale refinement network to improve the connectivity of preliminary segmentation on both normal and pathological cases. We reason that since it is difficult to derive a single model to accomplish the

task, refinement can be done to the existing segmentation. Compared to other similar GAN-based medical segmentation models, we have several novel improvements. Specifically, *tanh* is used as the final activation function in the generator to remove or add pixels to the preliminary labels guided by two centreline objective functions. The refined labels are then dilated using a fixed-size kernel and then times with the CT scan image before feeding into the discriminator. The dilation helps expand the visual field of the discriminator, which we assume could better help it distinguish real and fake pairs. We let the discriminator take image patches instead of the complete image because this allows only penalizing false synthesized structure at the local scale. We evaluate our model on two datasets: the BAS dataset, and our in-house dataset containing 25 cases of both cystic fibrosis and COVID-19, achieving more than 15% improvement in detected length ratio, detected branch ratio and false negative rate. The refinement pipeline also works on preliminary segmentation of other models, suggested by rises of more than 10% in the metrics mentioned above. Figures of refined results showed the discontinuity is fixed by our model, making the model more visually interpretable. We also did an ablation study to analyze the contribution of each component in our refinement scheme.

The main contributions of this paper can be summarised as follows:

- Our method provides a new angle for tackling discontinuity in airway segmentation. Instead of delineating the airway right from the start, the refinement model learns to add or remove pixels from the initial segmentation, aiming for better continuity. Moreover, the proposed refinement pipeline can extend to any existing segmentation models.
- Our method utilizes patch-scale discriminators to help the generator better focus on tiny structures.
- Two novel centreline-based loss functions are implemented to help the generator model maintain the continuity of refined results.
- The refinement pipeline is also tested on pathological cases, which were neglected by previous research, and achieves state-of-the-art performance.

II. RELATED WORKS

A. Airway Segmentation

The birth of the U-Net family [5][6][7][14] shifted the trend in medical image segmentation, and encoding-decoding-based architectures have dominated the field since then. Many deep-learning models have been proposed to segment the human airway structure and some of them have already achieved decent results in terms of IoU, detected length ratio and detected branch ratio. Qin et al. [12] proposed the two-step AirwayNet to maintain the high performance of the CNN on segmenting peripheral bronchioles. Zheng et al. [13] proposed WingsNet with group supervision to enhance the learning of small structures by CNN. They also designed a new objective function termed general union loss to address the imbalance between large and small airways. Charbonnier et al. [8] proposed a

ConvNet to detect and remove airway segmentation leakage. They came up with a way to combine segmentation generated by varying parameters to increase the length detected and reduce leakage. Jin et al. [9] used a 3-D FCN to produce high-quality labels from incomplete ones. They also employed a graph-based refinement incorporating fuzzy connectivity and skeletonisation. Wang et al. [11] designed a novel radial distance loss function based on distance transform that helps the network recover tiny tubular structures. Nonetheless, the problem of discontinuous predictions and miss detected tiny branches still exists.

B. Transformer-based medical segmentation

Transformers were originally proposed for NLP-related tasks due to their ability to encode long-range dependencies, but a recent study [15] showed that the architecture can also work with images. Since then, we have witnessed a surge of transformers applications in the medical imaging domain. For 3-D segmentation tasks, Wang et al. [16] proposed TransBTS which positioned a transformer module in between an encoder and a decoder as the bottleneck layer. Hatamizadeh et al. [17] introduced a U-Net Transformer (UNETR) that uses a transformer as the encoding part of the U-Net. Li et al. [18] proposed a Squeeze-and-Expansion Transformer where a squeezed attention block regularizes the self-attention module, and an expansion block learns diversified representations. Liu et al. [19] proposed a hierarchical transformer which adds a shifted window scheme to the multi-head attention (MSA) module. Unlike our methods, all previous work used the transformer module as a generator, not as a discriminator.

C. Adversarial-based medical segmentation

GAN-based segmentation has gained a lot of momentum in the field of medical imaging in recent years. Zhang et al. [20] used a modified 2-D dense U-Net to generate initial predictions of the airway and then employed a series of morphological operations to extract the small airways. A 3-D dense U-net is then used to learn from the sample of small airways using adversarial training with a cGAN. Zhao et al. [21] proposed a generative adversarial learning model with large receptive fields using the dilated residual block as the generator and a multi-layer CNN with residual blocks as the discriminator. Guo et al. [22] used a dense U-Net with an inception module as the generator and a multi-layer CNN as the discriminator. Park et al. [23] designed an M-GAN which also consists of a multi-layer CNN with residual blocks as the discriminator. Different from our patch-scale approach, despite there being some variations in the structure, previous works in medical segmentation all let the discriminator take in the complete image. Some of them have a complex multi-stage pipeline and didn't achieve competitive results compared with others.

III. METHODOLOGY

This section details our novel refinement method, including a generator \mathcal{G} and a discriminator \mathcal{D} . The generator takes in the preliminary segmentation z_i along with its corresponding

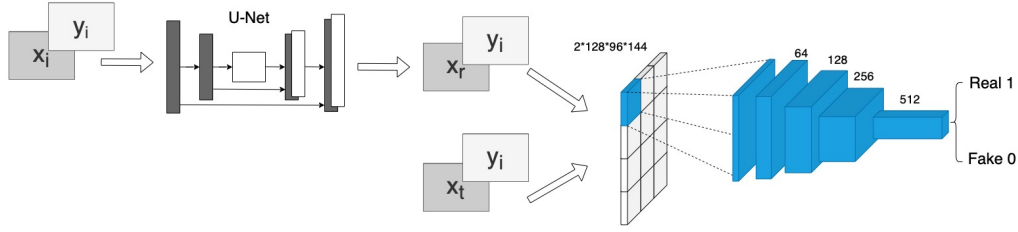


Fig. 2: The structure of the PatchGAN-based refinement model: U-Net with multi-scale supervision outputs the refined segmentation which is then fed into the PatchGAN discriminator that has five convolution layers. The channel number is denoted on each feature map.

CT image y_i and outputs a refined label $x_r = \mathcal{G}(y_i, x_i)$. The discriminator \mathcal{D} then tries to distinguish the $y_i \cdot (x_r \oplus k)$ from the $y_i \cdot (x_t \oplus k)$, where k is a kernel of size $5 \times 5 \times 5$, and x_t is the ground truth.

A. Generator

A 3-D U-Net [24][6] with multi-scale deep supervision is adopted [25] as the generator to segment the airway structure. CT images and preliminary labelling are combined into a 2-channel input and cut into patches with a dimension of $128 \times 96 \times 144$ before feeding into the generator. Preliminary labelling is generated using a small shallow version of U-net [26] because it is light and fast to train. The metrics describing the preliminary results are listed in Table I. The final activation layer is changed to \tanh instead of sigmoid since \tanh produces output that lies in the range $[-1, 1]$ and we set 0 as the threshold. For output smaller than zero, it is classified as -1 which aims to remove the false positive region in the preliminary labels; For output larger than zero, it is classified as 1 which aims to remove the false negative region in the preliminary labels. Specific loss functions are used to maintain the connectivity of the refinement which will be discussed in a later section.

B. Discriminator

Since previous work in medical segmentation has never tried to use discriminators on the scale of patches, we would like to test two types of them. One is the PatchGAN [27], which assumes the pixels separated by a patch distance are independent, and it penalizes structure at the scale of patches. The other one is the vision transformer[15], which models an image as a sequence of patches and focuses on the long-range dependencies between them. We hypothesized that if the discriminator can better distinguish the ground truth from the refined labels, then the generator can be better trained to focus on small-scale structures and therefore less breakage in the peripheral bronchioles. Two different discriminators are tested in our paper. First, A Markovian discriminator is utilized to distinguish a refined label from a true label. Specifically, both refined labels and true labels are dilated using a kernel of size $5 \times 5 \times 5$ and then timed with the corresponding CT images prior to feeding into the discriminator, which then tries to classify each $70 \times 70 \times 70$ patch as a synthesized label or ground truth. Second, We adopted a ViT-small(number of

layers = 12, Hidden Size = 768, MLP size = 3072, heads = 12) as our discriminator and change the \tanh in the MLP head to LeakyReLU with negative slope set to 0.2, and specified the patch size to be $32 \times 38 \times 36$.

C. Loss Functions

We use a hybrid loss function to train the refinement model. Specifically, the GAN adversarial loss is incorporated with Dice[7], cl-Dice[28] and Continuity and Completeness F-score (CCF) [29] defined as follows:

$$\text{Dice} = \frac{2 \sum_{i=1}^N p_i g_i}{\sum_{i=1}^N p_i^2 + \sum_{i=1}^N g_i^2} \quad (1)$$

where $p_i \in P$ is the predicted binary segmentation and $g_i \in G$ is the ground truth binary volume. The summation is taken over N voxels. To maintain the topological integrity of the predicted airway labels, we used clDice defined as:

$$\text{clDice} = \frac{2 \times T_{\text{prec}} \times T_{\text{sens}}}{T_{\text{prec}} + T_{\text{sens}}} \quad (2)$$

where *Topology precision* $T_{\text{prec}} = \frac{|S_P \cap V_L|}{|S_P|}$ and *Topology sensitivity* $T_{\text{sens}} = \frac{|S_L \cap V_P|}{|S_L|}$. V_L represents the ground truth mask and V_P represents the predicted mask. S is the skeletonised version of V . Dice and clDice are together in the following manner:

$$L_D = (1 - \alpha)(1 - \text{Dice}) + \alpha(1 - \text{clDice}) \quad (3)$$

where $\alpha \in [0, 0.5]$ is a weight parameter. To further enhance the centreline detection, we employed another objective function focused on continuity and completeness:

$$\begin{aligned} L_{CCF} &= 1 - C \\ &= 1 - \frac{\sum X \cdot Y_{CL}}{\sum Y_{CL}} \end{aligned} \quad (4)$$

where X is the predicted airway labels and Y_{CL} is the centreline of the ground truth. L1 loss is used to maintain the overall segmentation accuracy.

$$L_1 = |\sigma(x_i) - y_i| \quad (5)$$

The three loss functions described above are combined in the following manner across each layer j of supervision:

$$L_j = \alpha L_1 + \beta L_{CCF} + \gamma L_D + \delta L_{cGAN} \quad (6)$$

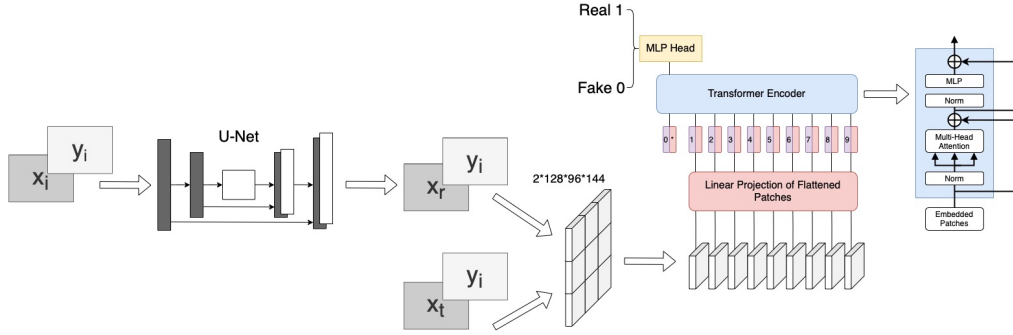


Fig. 3: The structure of adversarial ViT-based refinement model: U-Net with multi-scale supervision outputs the refined segmentation which is then fed into the ViT. The ViT splits the image into patches and embeds them into a set of encoded vectors of fixed dimension. The position of each patch is embedded along with the encoded vector.

where α , β , γ and δ are weight parameters with range $[0, 1.0]$. The total loss over all layers of supervision in the generator is combined with the GAN adversarial loss:

$$L_{cGAN}(G, D) = \mathbb{E}_{x,y}[\log D(x, y)] + \mathbb{E}_{x,z}[\log G(x, z)] \quad (7)$$

$$L = \phi_1 L_{layer1} + \phi_2 L_{layer2} + \phi_3 L_{layer3} + \phi_4 L_{final} \quad (8)$$

where ϕ_1 to ϕ_4 are weight parameters for each layer.

IV. EXPERIMENTS AND RESULTS

A. Dataset

We trained and evaluated our model on the Binary Airway Segmentation (BAS) dataset which contains 90 CT scans with 20 of them from the training set of EXACT'09 [4]¹ and 70 of them are from LIDC-IDRI [30]. The original LIDC-IDRI dataset includes 1018 cases but with no airway annotations. [12] and [13] selected 70 cases whose slice thickness is less than or equal to 0.625mm and carefully annotated them². We split the 90 scans into 72 for training and 18 for testing. In addition, we also tested our model on the in-house fibrosis datasets (25 cases) and COVID-19 datasets (25 cases) respectively.

B. Implementation Details

The model was implemented using PyTorch and trained on NVIDIA GeForce RTX 3090 for 150 epochs. For the generator part, we used an *Adam* solver with a learning rate = 0.001, and the learning rate was set to decay by half at the 50th, 80th, 100th and 120th epochs. For the discriminator part, we used an *Adam* solver with learning rate = 0.001 betas = 0.5, 0.999. The backpropagation was first performed on the discriminator and then on the generator. Data augmentation was performed on the fly via random horizontal and vertical flips ($p=0.5$).

During the inference on the test dataset, the input patches are extracted using a sliding window manner with 50% of overlap in the x,y, and z directions. Patches of binary prediction are stitched back to the full image and then the largest connected component is preserved to reduce noise.

C. Evaluation Metrics

Given the binary voxel-wise prediction X and the ground truth Y , we adopt IoU and Dice coefficient to measure the overall segmentation accuracy as well as other metrics specific for tree-like structures, defined as follows:

IoU and Dice Coefficient both measure the proportion of overlapping between the prediction and the ground truth:

$$IoU = \frac{XY}{X + Y - XY} \quad (9)$$

$$Dice = \frac{2XY}{X + Y} = \frac{2IoU}{IoU + 1} \quad (10)$$

Detected Length Ratio (DLR) measures the proportion of detected branch length with respect to that of the ground truth:

$$DLR = \frac{L_X}{L_Y} \quad (11)$$

where L_X is the total length of the correctly detected airway, L_Y is the total length of the airway in the ground truth.

Detected Branch Ratio (DBR) measures the proportion of detected branch number with respect to that of the ground truth:

$$DBR = \frac{N_X}{N_Y} \quad (12)$$

where N_X is the total number of correctly detected airway branches, N_Y is the number of branches in the ground truth. In this study, branches with the intersection over union (IoU) score greater than 0.8 are referred to be correctly identified.

Precision refers to the fraction of correctly identified airway voxels among the predicted airway:

$$Precision = \frac{TP}{TP + FP} \quad (13)$$

where TP and FP are the numbers of true positive voxels and false positive voxels.

Leakage measures the proportion of total false positives with respect to the ground truth annotations:

$$Leakage = \frac{V_X}{V_Y} \quad (14)$$

where V_X is the volume of false-positive predictions, V_Y is the volume of ground truth annotations.

¹ Accessible at <http://image.diku.dk/exact/>

² Accessible at <https://geronsushi.github.io/lung.html>

Airway Missing Ratio (AMR) measures the proportion of total undetected airways (false negatives) with respect to the ground truth annotations:

$$AMR = \frac{FN}{V_Y} \quad (15)$$

where FN is the volume of false-negative predictions, V_Y is the volume of ground truth annotations.

D. Segmentation Results

We use seven evaluation metrics including intersection over union (IoU), dice coefficient, detected length ratio (DLR), detected branch ratio (DBR), precision, leakage and false negative rates (AMR) to evaluate the performance of our model comprehensively. Furthermore, we perform Wilcoxon signed-rank test ($\alpha = 0.01$) for statistical analysis. **Comparison on BAS dataset:** Our proposed method achieved state-of-the-art performance on BAS (Table II and Figure 4, 5) with 0.8902 DLR, 0.8439 DBR and 0.05441 AMR. WingsNet achieves the highest IoU (0.8544) and voxel-wise precision (0.9458) among all models. NaviAirway has the lowest AMR (0.0413) while the model proposed by Wang et al. suffers from high leakage (0.3070). NaviAirway and the model proposed by Wang et al. also have competitive performance in DLR and DBR.

Comparison on in-house fibrosis dataset: All models performance decreases drastically in the fibrosis cases (Table II and Figure 4, 5). Notwithstanding, our model still achieves the highest DLR (0.7242), DBR (0.6550) and lowest AMR (0.08232). WingsNet and the model proposed by Wang et al. achieve similar results on DLR and DBR, but WingsNet has a better IoU score. NaviAirway obtains the highest IoU while unexpectedly achieving a poor performance on maintaining continuity with 0.5994 DLR and 0.5148 DBR.

Comparison on in-house COVID-19 dataset: All models perform slightly better compared to them on the BAS dataset (Table II and Figure 4, 5). The proposed method achieves the best DLR (0.9104), DBR (0.8772) and AMR (0.0281) in the COVID-19 cases. WingsNet achieves the second highest DLR (0.9073) and DBR (0.8682) followed by NaviAirway with 0.9394 DLR and 0.8729 DBR. WingsNet also achieves highest IoU (0.9176), Dice (0.9566) and precision (0.9683)

Refined segmentation on other three models: To demonstrate our refinement pipeline can be extended to other models, we refined all three other aforementioned models (WingsNet, NaviAirway and the model proposed by Wang et al.). Overall, all three models' performance on all three datasets (BAS, fibrosis and COVID-19) improved significantly with DLR and DBR increasing more than 10% on average (Table III). The IoU and Dice decrease a little as a trade-off in all scenarios with some even not considered to be statistically significant. The false negative ratio is also reduced significantly in all cases. Notably, the improvement on these three models is not as much as the refinement of our own preliminary results. Figure 6 to 8 provide a zoom-in illustration of the effect of our refinement visually.

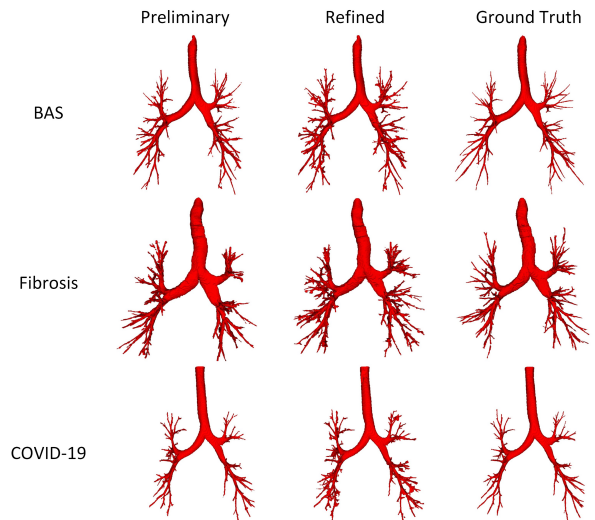


Fig. 4: Visualization of preliminary segmentation, refined segmentation and the ground truth on BAS (CASE02) and our in-house dataset (162_01 in fibrosis and RM451 in COVID-19)

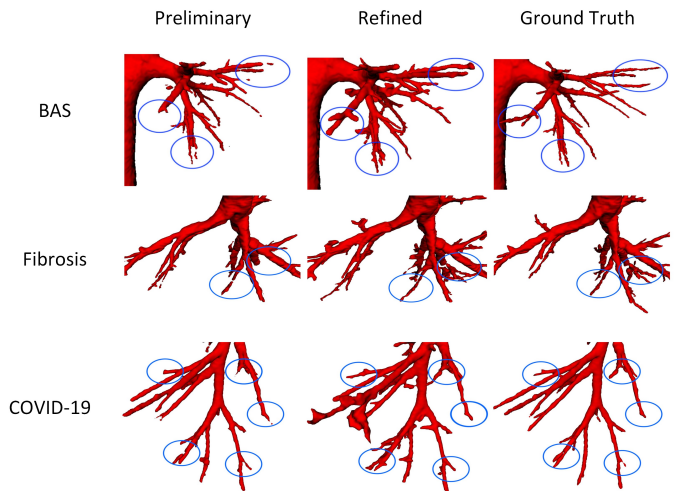


Fig. 5: Visualization of the zoomed-in region in preliminary segmentation, refined segmentation and the ground truth on BAS (CASE02) and our in-house dataset (162_01 in fibrosis and RM451 in COVID-19)

E. Ablation Study

We run ablation studies to isolate the effect of each component in our refinement model as shown in Table IV including 3-D U-Net + PatchGAN with dilation (BL), BL + cDice, BL + CCF, BL + CCF with multi-scale supervision, BL+cDice with multi-scale supervision, BL+cDice+CCF with multi-scale supervision and BL (PatchGAN is replaced with ViT)+cDice+CCF with multi-scale supervision. By adopting cDice, all seven metrics are slightly improved (roughly 1.0% average gain). When cDice is replaced with CCF, IoU, Dice and leakage become worse while the rest four metrics are improved drastically by more than 5.0% on average. The incorporation of multi-scale supervision helps

TABLE I: Preliminary segmentation results

	Model	IoU	Dice	DLR	DBR	Precision	Leakages	AMR
Valid	small U-Net	0.8372±0.0752	0.9093±0.0505	0.7346±0.1419	0.6425±0.1555	0.9344±0.0314	0.0621±0.0269	0.1117±0.0762
Fibrosis	small U-Net	0.7911±0.0532	0.8823±0.0349	0.5616±0.1076	0.4829±0.1218	0.9296±0.0294	0.0657±0.0362	0.1568±0.0637
COVID	small U-Net	0.8637±0.10165	0.9228±0.0756	0.7173±0.1507	0.6302±0.1507	0.9566±0.0134	0.0407±0.0137	0.1008±0.1079

TABLE II: Comparison experiments on different datasets

	Model	IoU↓	Dice↓	DLR↑	DBR↑	Precision↓	Leakage↑	AMR↓
Valid	Wang et al. [11]†	0.7330±0.0786‡	0.8434±0.0554‡	0.8505±0.1227‡	0.7858±0.1420‡	0.7636±0.0737‡	0.3070±0.1412‡	0.0507±0.0619
	WingsNet [13]*	0.8544±0.0673‡	0.9120±0.0422‡	0.8698±0.1175‡	0.8166±0.1305‡	0.9458±0.0271‡	0.0529±0.0300‡	0.1002±0.0769‡
	NaviAirway [31]*	0.8348±0.0335	0.9096±0.0200	0.8734±0.0715	0.8099±0.0950‡	0.8672±0.0406	0.1500±0.0536	0.0413±0.0304
	Unet+PatchGAN	0.8150±0.0519	0.8971±0.0330	0.8828±0.1012	0.8337±0.1263	0.8556±0.0393	0.1620±0.0522	0.0544±0.0525
	Unet+ViT	0.8132±0.0518	0.8961±0.0334	0.8902±0.0967	0.8439±0.1261	0.8600±0.0401	0.1549±0.0539	0.0623±0.0504
Fibrosis	Wang et al. [11]†	0.6979±0.0647‡	0.8203±0.0462‡	0.6961±0.0924‡	0.6261±0.1117‡	0.7468±0.0773‡	0.3272±0.1445‡	0.0823±0.0388
	WingsNet [13]*	0.8052±0.0539‡	0.8910±0.0440‡	0.6951±0.0977‡	0.6198±0.1175‡	0.9505±0.0116‡	0.0438±0.0112‡	0.1595±0.0576‡
	NaviAirway [31]*	0.8074±0.0533‡	0.8924±0.0440‡	0.5994±0.1440‡	0.5148±0.1490‡	0.9247±0.0165‡	0.0714±0.0188‡	0.1345±0.0645‡
	Unet+PatchGAN	0.7481±0.0678	0.8541±0.0464	0.7157±0.1067	0.6437±0.1195	0.8035±0.0775	0.2374±0.1286	0.0823±0.0332
	Unet+ViT	0.7272±0.0631	0.8405±0.0436	0.7242±0.1096	0.6550±0.1266	0.7879±0.0816	0.2606±0.1401	0.0916±0.0325
COVID	Wang et al. [11]†	0.7433±0.1010‡	0.8481±0.0798‡	0.8487±0.1320‡	0.7993±0.1409‡	0.7749±0.0736‡	0.2843±0.1500‡	0.0541±0.1035‡
	WingsNet [13]*	0.9176±0.0363‡	0.9566±0.0209‡	0.9073±0.0647	0.8682±0.0831	0.9683±0.0204‡	0.0311±0.0203‡	0.0544±0.0283‡
	NaviAirway [31]*	0.8861±0.0298‡	0.9394±0.0171‡	0.8729±0.0792‡	0.8060±0.1034‡	0.9100±0.0245‡	0.0970±0.0316‡	0.0286±0.0239
	Unet+PatchGAN	0.8292±0.0335	0.9063±0.0203	0.8911±0.0827	0.8443±0.1044	0.8506±0.0413	0.1741±0.0575	0.0281±0.0258
	Unet+ViT	0.8090±0.0483	0.8936±0.0307	0.9104±0.0751	0.8772±0.0987	0.8354±0.0458	0.1933±0.0705	0.0378±0.0231

* refers to results obtained from open-source implementations with model weights provided.

† refers to reproduced results.

‡ represents statistical significance (with Wilcoxon signed-rank test $p < 0.01$) compared with the proposed method.

TABLE III: Refined segmentation results

	Model	IoU↓	Dice↓	DLR↑	DBR↑	Precision↓	Leakages↑	AMR↓
Valid	Wang et al. [11]†	0.7330±0.0786‡	0.8434±0.0554‡	0.8505±0.1227‡	0.7858±0.1420‡	0.7636±0.0737‡	0.3070±0.1412‡	0.0507±0.0619‡
	Refined Wang et al.	0.7136±0.1000	0.8284±0.0763	0.9093±0.1263	0.8700±0.1380	0.7341±0.0793	0.3552±0.1281	0.0423±0.0960
	WingsNet [13]*	0.8544±0.0673	0.9200±0.0422	0.8698±0.1175‡	0.8166±0.1305‡	0.9458±0.0271‡	0.0529±0.0300‡	0.1002±0.0769‡
	Refined WingsNet	0.8504±0.0651	0.9177±0.0409	0.9050±0.1032	0.8621±0.1230	0.9331±0.0303	0.0668±0.0347	0.0927±0.0752
	NaviAirway [31]*	0.8348±0.0335‡	0.9096±0.0200‡	0.8734±0.0715‡	0.8099±0.0950‡	0.8672±0.0406‡	0.1500±0.0536‡	0.0413±0.0304‡
Fibrosis	Wang et al. [11]†	0.6979±0.0647‡	0.8203±0.0462‡	0.6961±0.0924‡	0.6261±0.1117‡	0.7468±0.0773‡	0.3272±0.1445‡	0.0823±0.0388
	Refined Wang et al.	0.6528±0.0925	0.7859±0.0722	0.8007±0.0847	0.7399±0.1042	0.6736±0.0951	0.4953±0.2456	0.0456±0.0277
	WingsNet [13]*	0.8052±0.0539‡	0.8910±0.0340‡	0.6951±0.0977‡	0.6198±0.1175‡	0.9505±0.0116‡	0.0438±0.0113‡	0.1595±0.0576‡
	Refined WingsNet	0.8035±0.0515	0.8901±0.0326	0.7318±0.1012‡	0.6638±0.1221‡	0.9341±0.0159	0.0604±0.0163	0.1480±0.0565
	NaviAirway [31]*	0.8074±0.0533‡	0.8924±0.0340‡	0.5994±0.1440‡	0.5148±0.1490‡	0.9247±0.0165‡	0.0714±0.0188‡	0.1345±0.0645‡
COVID	Wang et al. [11]†	0.7433±0.1010‡	0.8481±0.0798‡	0.8487±0.1320‡	0.7993±0.1409‡	0.7749±0.0736‡	0.2843±0.1500‡	0.0541±0.1035‡
	Refined Wang et al.	0.7408±0.0566	0.8498±0.0392	0.9538±0.0435	0.9316±0.0603	0.7462±0.0562	0.3453±0.1152	0.0098±0.0106
	WingsNet [13]*	0.9176±0.0363‡	0.9566±0.0209‡	0.9073±0.0647‡	0.8682±0.0831‡	0.9683±0.0204‡	0.0311±0.0203‡	0.0544±0.0283‡
	Refined WingsNet	0.8971±0.0345	0.9454±0.0200	0.9571±0.0575	0.9409±0.0778	0.9424±0.0266	0.0588±0.0297	0.0510±0.0259
	NaviAirway [31]*	0.8861±0.0298‡	0.9394±0.0171‡	0.8729±0.0792‡	0.8060±0.1034‡	0.9100±0.0245‡	0.0970±0.0316‡	0.0286±0.0239‡
COVID	Refined NaviAirway	0.8725±0.0315	0.9316±0.0186	0.9153±0.0724	0.8732±0.0997	0.8904±0.0295	0.1218±0.0407	0.0223±0.0214

* refers to results obtained from open-source implementations with model weights provided.

† refers to reproduced results.

‡ represents statistical significance (with Wilcoxon signed-rank test $p < 0.01$) compared with the refined results.

the model guided by CCF and cl-Dice promote in all seven metrics. Finally, the best performance in DLR (0.8902) and DBR (0.8439) is achieved when CCF, cl-Dice and multi-scale supervision are combined with ViT.

V. DISCUSSION AND CONCLUSION

In this paper, we proposed a novel adversarial-based refinement model using \tanh as the final activation function and trained the network using objective functions clDice and CCF

that focus on the continuity of the airway. The refinement model corrects breakage and adds missing branches in the preliminary segmentation generated by other networks such as U-Net.

We evaluated our model on two datasets: the BAS dataset, and our in-house dataset containing 25 cases of cystic fibrosis and 25 cases of COVID-19. By comparing preliminary results in Table I and refined results in Table II, we can find that our method significantly reduces false negatives and increase

TABLE IV: Ablation study of the proposed model.

Model	IoU	Dice	DLR	DBR	Precision	Leakages	AMR
U-Net+PatchGAN+dilation(BL)	0.8274±0.0563	0.9044±0.0355	0.7936±0.1303	0.7088±0.1557	0.8866±0.0405	0.1215±0.0504	0.0730±0.0622
BL+clDice	0.8325±0.0465	0.9079±0.0294	0.8059±0.1285	0.7324±0.1525	0.8895±0.0313	0.1178±0.0400	0.0693±0.0608
BL+ccf	0.7133±0.0854	0.8295±0.0631	0.8526±0.1148	0.7947±0.1474	0.7441±0.0880	0.3519±0.2151	0.0516±0.0541
BL+ccf+multi-scale	0.7701±0.0522	0.8691±0.0343	0.8420±0.1277	0.7788±0.1542	0.8101±0.0484	0.2266±0.0761	0.0573±0.0600
BL+clDice+multi-scale	0.8342±0.0670	0.9080±0.0427	0.8352±0.1156	0.7671±0.1421	0.8969±0.0478	0.1082±0.0578	0.0781±0.0565
BL+ccf+ clDice + multi-scale	0.8150±0.0519	0.8971±0.0330	0.8828±0.1012	0.8337±0.1263	0.8556±0.0393	0.1620±0.0522	0.0544±0.0525
BL(ViT) + ccf + cl_dice + multi-scale	0.8133±0.0518	0.8961±0.0334	0.8902±0.0967	0.8439±0.1261	0.8600±0.0401	0.1549±0.0539	0.0623±0.0505

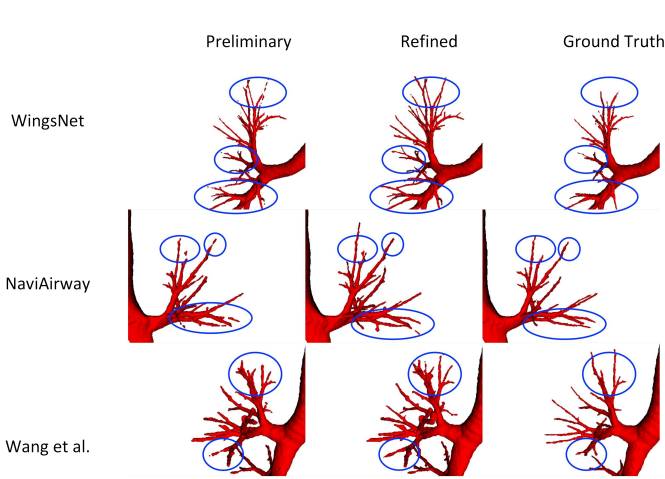


Fig. 6: Zoom in on bronchioles of CASE02 in EXACT'09 test set; From top to bottom row are results from WingsNet, NaviAirway and Wang et al. respectively; From left to right column are initial segmentation of their models, refined segmentation and ground truth. Blue circles indicate breakages in the preliminary segmentation, but are later fixed by the refinement model

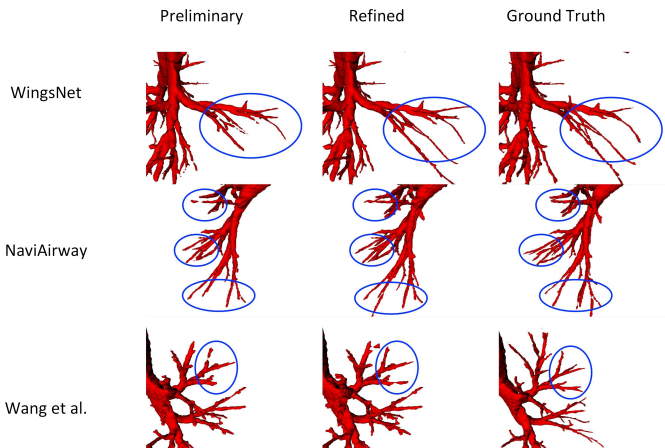


Fig. 7: Zoom in on bronchioles of Case 162_01 in fibrosis test set; From top to bottom row are results from WingsNet, NaviAirway and Wang et al. respectively; From left to right column are initial segmentation of their models, refined segmentation and ground truth. Blue circles indicate breakages in the preliminary segmentation, but are later fixed by the refinement model

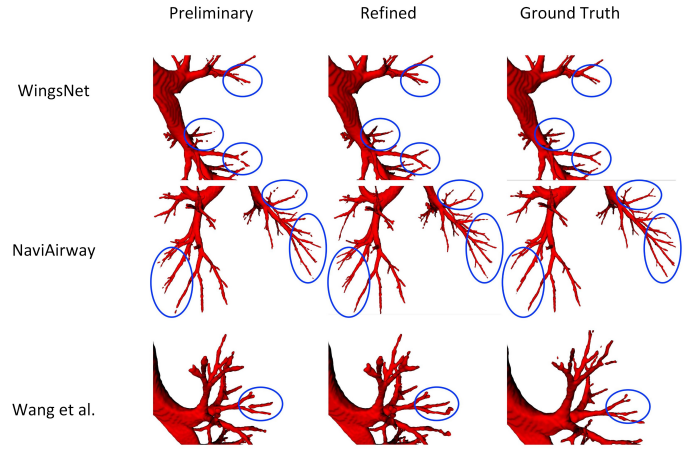


Fig. 8: Zoom in on bronchioles of Case RM451 in the COVID test set; From top to bottom row are results from WingsNet, NaviAirway and Wang et al. respectively; From left to right column are initial segmentation of their models, refined segmentation and ground truth. Blue circles indicate breakages in the preliminary segmentation, but are later fixed by the refinement model

the length and number of detected branches in all three test datasets. In Figures 4 to 8, we use blue circles to indicate breakage and bronchioles missed in preliminary segmentation but later successfully detected in the refined results. Airway segmentation completeness is essential for the clinical implementation of the algorithm since it can provide biomarkers for evaluating the severity of lung diseases. For example, traction bronchiectasis [32][33] and airway tapering [34] are useful biomarkers in the prognosis of cystic fibrosis. The ability of our model to maintain the local connectivity and thereby maximize the completeness is desirable for clinical use since methods to evaluate the airway assume disconnected branches are removed when retrieving the largest connected component.

There are also limitations in our current approach. First, the model is trained on a specific set of preliminary segmentation generated using a small U-Net. Therefore, The improvement in the preliminary segmentation produced by the same network (small U-Net) is higher than in the other three models (Wang et al., WingsNet and NaviAirway). Its ability to refine is also constrained by the quality of the preliminary results, which is also suggested in Table. III that better initial results generally lead to better refinement. To solve this issue in the future, we will probably train the model using preliminary segmentation generated by randomly masking out ground truth. Second,

although airway continuity is maintained, some peripheral bronchioles are over-segmented after repairing which is also reflected by the higher leakage. The leakage is more recognizable in the fibrosis dataset than it is in the BAS and COVID-19 datasets. Another interesting observation we noticed from figures 4 to 8 is that sometimes the predictions have detected correct airway branches not shown in the ground truth. This also could explain why the IoU and Dice decrease a little while leakage rises after refinement.

In conclusion, we have demonstrated that patch-scale discriminators can help improve airway segmentation in terms of better connectivity and lower false negative rates. This refinement pipeline can also be extended to other models and segmentation tasks in the future.

REFERENCES

- [1] D. Aykac, E. Hoffman *et al.*, “Segmentation and analysis of the human airway tree from three-dimensional x-ray ct images,” *IEEE Transactions on Medical Imaging*, vol. 22, no. 8, pp. 940–950, 2003.
- [2] J. Tschirren, E. Hoffman *et al.*, “Intrathoracic airway trees: segmentation and airway morphology analysis from low-dose ct scans,” *IEEE Transactions on Medical Imaging*, vol. 24, no. 12, pp. 1529–1539, 2005.
- [3] M. W. Graham, J. D. Gibbs *et al.*, “Robust 3-d airway tree segmentation for image-guided peripheral bronchoscopy,” *IEEE Transactions on Medical Imaging*, vol. 29, no. 4, pp. 982–997, 2010.
- [4] P. Lo, B. van Ginneken *et al.*, “Extraction of airways from ct (exact’09),” *IEEE Transactions on Medical Imaging*, vol. 31, no. 11, pp. 2093–2107, 2012.
- [5] O. Ronneberger, P. Fischer, and T. Brox, “U-net: Convolutional networks for biomedical image segmentation,” in *Medical Image Computing and Computer-Assisted Intervention – MICCAI 2015*, N. Navab, J. Hornegger *et al.*, Eds. Cham: Springer International Publishing, 2015, pp. 234–241.
- [6] Özgün Çiçek, A. Abdulkadir *et al.*, “3d u-net: Learning dense volumetric segmentation from sparse annotation,” in *Medical Image Computing and Computer-Assisted Intervention – MICCAI 2016*, S. Ourselin, L. Joskowicz *et al.*, Eds. Cham: Springer International Publishing, 2016, pp. 424–432.
- [7] F. Milletari, N. Navab, and S.-A. Ahmadi, “V-net: Fully convolutional neural networks for volumetric medical image segmentation,” in *2016 Fourth International Conference on 3D Vision (3DV)*, 2016, pp. 565–571.
- [8] J.-P. Charbonnier, E. M. van Rikxoort *et al.*, “Improving airway segmentation in computed tomography using leak detection with convolutional networks,” *Medical Image Analysis*, vol. 36, pp. 52–60, 2017. [Online]. Available: <https://www.sciencedirect.com/science/article/pii/S136184151630202X>
- [9] D. Jin, Z. Xu *et al.*, “3d convolutional neural networks with graph refinement for airway segmentation using incomplete data labels,” in *Machine Learning in Medical Imaging*, Q. Wang, Y. Shi *et al.*, Eds. Cham: Springer International Publishing, 2017, pp. 141–149.
- [10] Q. Meng, H. R. Roth *et al.*, “Tracking and segmentation of the airways in chest ct using a fully convolutional network,” in *Medical Image Computing and Computer-Assisted Intervention – MICCAI 2017*, 2017, pp. 198–207.
- [11] C. Wang, Y. Hayashi *et al.*, “Tubular structure segmentation using spatial fully connected network with radial distance loss for 3d medical images,” in *Medical Image Computing and Computer Assisted Intervention – MICCAI 2019*, D. Shen, T. Liu *et al.*, Eds. Cham: Springer International Publishing, 2019, pp. 348–356.
- [12] Y. Qin, Y. Gu *et al.*, “Airwaynet-se: A simple-yet-effective approach to improve airway segmentation using context scale fusion,” in *2020 IEEE 17th International Symposium on Biomedical Imaging (ISBI)*, 2020, pp. 809–813.
- [13] H. Zheng, Y. Qin *et al.*, “Alleviating class-wise gradient imbalance for pulmonary airway segmentation,” *IEEE Transactions on Medical Imaging*, vol. 40, pp. 2452–2462, 9 2021.
- [14] F. Isensee, P. F. Jaeger *et al.*, “nnu-net: a self-configuring method for deep learning-based biomedical image segmentation,” *Nature Methods*, vol. 18, pp. 203–211, 2 2021.
- [15] A. Dosovitskiy, L. Beyer *et al.*, “An image is worth 16x16 words: Transformers for image recognition at scale,” in *International Conference on Learning Representations*, 2021. [Online]. Available: <https://openreview.net/forum?id=YicbFdNTTy>
- [16] W. Wang, C. Chen *et al.*, “Transbts: Multimodal brain tumor segmentation using transformer,” in *Medical Image Computing and Computer Assisted Intervention – MICCAI 2021: 24th International Conference, Strasbourg, France, September 27–October 1, 2021, Proceedings, Part I*. Berlin, Heidelberg: Springer-Verlag, 2021, p. 109–119.
- [17] A. Hatamizadeh, Y. Tang *et al.*, “Unetr: Transformers for 3d medical image segmentation,” in *2022 IEEE/CVF Winter Conference on Applications of Computer Vision (WACV)*. IEEE, 1 2022, pp. 1748–1758.
- [18] S. Li, X. Sui *et al.*, “Medical image segmentation using squeeze-and-expansion transformers,” in *Proceedings of the Thirtieth International Joint Conference on Artificial Intelligence*. International Joint Conferences on Artificial Intelligence Organization, 8 2021, pp. 807–815.
- [19] Z. Liu, Y. Lin *et al.*, “Swin transformer: Hierarchical vision transformer using shifted windows,” in *2021 IEEE/CVF International Conference on Computer Vision (ICCV)*. IEEE, 10 2021, pp. 9992–10 002.
- [20] H. Zhang, M. Shen *et al.*, “Pathological airway segmentation with cascaded neural networks for bronchoscopic navigation,” in *2020 IEEE International Conference on Robotics and Automation (ICRA)*. IEEE, 5 2020, pp. 9974–9980.
- [21] H. Zhao, X. Qiu *et al.*, “High-quality retinal vessel segmentation using generative adversarial network with a large receptive field,” *International Journal of Imaging Systems and Technology*, vol. 30, pp. 828–842, 9 2020.
- [22] X. Guo, C. Chen *et al.*, “Retinal vessel segmentation combined with generative adversarial networks and dense u-net,” *IEEE Access*, vol. 8, pp. 194 551–194 560, 2020.
- [23] K.-B. Park, S. H. Choi, and J. Y. Lee, “M-gan: Retinal blood vessel segmentation by balancing losses through stacked deep fully convolutional networks,” *IEEE Access*, vol. 8, pp. 146 308–146 322, 2020.
- [24] O. Ronneberger, P. Fischer, and T. Brox, “U-net: Convolutional networks for biomedical image segmentation,” in *Medical Image Computing and Computer-Assisted Intervention – MICCAI 2015*, N. Navab, J. Hornegger *et al.*, Eds. Cham: Springer International Publishing, 2015, pp. 234–241.
- [25] C.-Y. Lee, S. Xie *et al.*, “Deeply-Supervised Nets,” in *Proceedings of the Eighteenth International Conference on Artificial Intelligence and Statistics*, ser. Proceedings of Machine Learning Research, G. Lebanon and S. V. N. Vishwanathan, Eds., vol. 38. San Diego, California, USA: PMLR, 09–12 May 2015, pp. 562–570. [Online]. Available: <https://proceedings.mlr.press/v38/lee15a.html>
- [26] A. Garcia-Uceda Juarez, H. A. W. M. Tiddens, and M. de Bruijne, “Automatic airway segmentation in chest ct using convolutional neural networks,” in *Image Analysis for Moving Organ, Breast, and Thoracic Images*, D. Stoyanov, Z. Taylor *et al.*, Eds. Cham: Springer International Publishing, 2018, pp. 238–250.
- [27] P. Isola, J.-Y. Zhu *et al.*, “Image-to-image translation with conditional adversarial networks,” in *2017 IEEE Conference on Computer Vision and Pattern Recognition (CVPR)*, 2017, pp. 5967–5976.
- [28] S. Shit, J. C. Paetzold *et al.*, “cldice - a novel topology-preserving loss function for tubular structure segmentation,” in *2021 IEEE/CVF Conference on Computer Vision and Pattern Recognition (CVPR)*, 2021, pp. 16 555–16 564.
- [29] Y. Nan, J. Del Ser *et al.*, “Fuzzy attention neural network to tackle discontinuity in airway segmentation,” 2022. [Online]. Available: <https://arxiv.org/abs/2209.02048>
- [30] S. G. Armato, G. McLennan *et al.*, “The lung image database consortium (lidc) and image database resource initiative (idri): A completed reference database of lung nodules on ct scans,” *Medical Physics*, vol. 38, pp. 915–931, 1 2011.
- [31] A. Wang, T. C. C. Tam *et al.*, “Naviarway: a bronchiole-sensitive deep learning-based airway segmentation pipeline,” 2022. [Online]. Available: <https://arxiv.org/abs/2203.04294>
- [32] S. L. Walsh, N. Sverzellati *et al.*, “Chronic hypersensitivity pneumonitis: high resolution computed tomography patterns and pulmonary function indices as prognostic determinants,” *European Radiology*, vol. 22, pp. 1672–1679, 8 2012.
- [33] —, “Connective tissue disease related fibrotic lung disease: high resolution computed tomographic and pulmonary function indices as prognostic determinants,” *Thorax*, vol. 69, no. 3, pp. 216–222, 2014. [Online]. Available: <https://thorax.bmj.com/content/69/3/216>
- [34] W. Kuo, A. Perez-Rovira *et al.*, “Airway tapering: an objective image biomarker for bronchiectasis,” *European Radiology*, vol. 30, pp. 2703–2711, 5 2020.